

# Journal Pre-proofs

Bi-functional carbon-based catalysts for unitized regenerative fuel cells

L.M. Rivera-Gavidia, I. Fernández de la Puente, M.A. Hernández-Rodríguez,  
V. Celorio, D. Sebastián, M.J. Lázaro, E. Pastor, G. García

PII: S0021-9517(20)30128-7

DOI: <https://doi.org/10.1016/j.jcat.2020.04.007>

Reference: YJCAT 13709

To appear in: *Journal of Catalysis*

Received Date: 5 October 2019

Revised Date: 16 February 2020

Accepted Date: 4 April 2020



Please cite this article as: L.M. Rivera-Gavidia, I. Fernández de la Puente, M.A. Hernández-Rodríguez, V. Celorio, D. Sebastián, M.J. Lázaro, E. Pastor, G. García, Bi-functional carbon-based catalysts for unitized regenerative fuel cells, *Journal of Catalysis* (2020), doi: <https://doi.org/10.1016/j.jcat.2020.04.007>

This is a PDF file of an article that has undergone enhancements after acceptance, such as the addition of a cover page and metadata, and formatting for readability, but it is not yet the definitive version of record. This version will undergo additional copyediting, typesetting and review before it is published in its final form, but we are providing this version to give early visibility of the article. Please note that, during the production process, errors may be discovered which could affect the content, and all legal disclaimers that apply to the journal pertain.

© 2020 Elsevier Inc. All rights reserved.

## Bi-functional carbon-based catalysts for unitized regenerative fuel cells

L.M. Rivera-Gavidia<sup>1</sup>, I. Fernández de la Puente<sup>1</sup>, M.A. Hernández-Rodríguez<sup>2</sup>, V. Celorio<sup>3,†</sup>, D. Sebastián<sup>3</sup>, M.J. Lázaro<sup>3</sup>, E. Pastor<sup>1\*</sup> and G. García<sup>1\*</sup>

<sup>1</sup>*Departamento de Química, IMN, Universidad de La Laguna, PO Box 456, E-38200, La Laguna, Santa Cruz de Tenerife, Spain*

<sup>2</sup>*Departamento de Física, MALTA Consolider Team, IMN, IUDEA, Universidad de La Laguna, PO Box 456, E-38200, La Laguna, Santa Cruz de Tenerife, Spain*

<sup>3</sup>*Instituto de Carboquímica, Miguel Luesma Castán 4, E-50018, Zaragoza, Spain.*

<sup>†</sup>*Current address: Diamond Light Source Ltd, Diamond House, Harwell Campus, Didcot, United Kingdom*

\* Corresponding authors:

E. Pastor: E-mail address: [epastor@ull.edu.es](mailto:epastor@ull.edu.es); Phone: +34922318071

G. García: E-mail address: [ggarci@ull.edu.es](mailto:ggarci@ull.edu.es); Phone: +34922318032

### Abstract

Alkaline unitized regenerative fuel cells (URFCs) could well be one of the energy sources in the next future. This technology has the potential to provide power to portable devices, transportation and stationary sectors. The bifunctional oxygen electrode plays a central role in catalytic activity and stability due to its slow kinetics under extremely oxidizing or reducing environments. With the aim to solve the principal catalytic problems at the bifunctional electrocatalysts, carbonaceous materials including carbon nanofibers (CNFs), graphitized mesoporous carbon (gCMK-3) and hydrazine-reduced graphene oxide (H-rGO) were synthesized, characterized and tested toward the oxygen evolution reaction (OER) and the oxygen reduction reaction (ORR) and compared to commercial carbon black (Vulcan), graphite, and glassy carbon (GC). Physicochemical characterization was conducted by X-ray diffraction (XRD), X-ray photoelectron spectroscopy (XPS), elemental analysis and Raman spectroscopy, meanwhile rotating ring-disk electrode (RRDE) was employed to determine the electrochemical activity and stability. Main results indicate that CNFs can act as a feasible catalyst for URFC applications.

**Keywords:** ORR; OER; URFC; Catalysis; Electrocatalysis; Graphene; RRDE.

## 1. Introduction

The so-called hydrogen economy is still being considered to promote the consumption of renewable and non-polluting energy sources. Hydrogen from the electrolysis of water can play the role of an energy carrier. Indeed, hydrogen is likely to become an important chemical energy carrier and eventually may become the principal chemical energy carrier [1–3]. The interconversions of electricity into chemicals and *viceversa* require electrochemical devices: electrolyzers are used to convert electricity and water into hydrogen, and H<sub>2</sub>/air polymer electrolyte fuel cells (PEMFCs) are used to convert hydrogen fuel back into electricity. Unitized regenerative fuel cells (URFCs), a combination of both technologies, offer new perspectives to further bring down investment costs in the near future and to open the way to mass production for domestic applications [4, 5]. This combination has the potential to be a near-zero emission energy supply system. In this respect, an URFC system is directly comparable to a secondary battery, especially in terms of user handling and the charging/discharging behavior [1,6].

At the present time, URFCs have not yet reached the level of development obtained with fuel cells and electrolyzers. Electrochemical performances still require additional optimization, both in terms of efficiency and long-term performances. In order to improve the round-trip efficiency of the URFC, one key issue is the fabrication of low-cost, stable and highly active bi-operational (bi-functional) oxygen electrode catalysts, which can be used for both oxygen reduction reactions (ORR) and oxygen evolution reactions (OER) [7,8]. Bi-operational electrocatalysts for URFC applications have been developed using a combination of unsupported metallic platinum and OER electrocatalysts such as ruthenium (oxide) and iridium (oxide) [8-12]. However, the high-cost, scarcity and the high corrosion rate (especially in water electrolysis mode) of the employed catalysts represents a great barrier for their insertion to the market [13]. Recent advances have shown great potential of carbonaceous materials combined with metal or metal oxide nanostructures as bifunctional catalysts for the oxygen electrode [14-21].

In this study, graphenic materials (GMs) obtained from graphene oxide reduction using hydrazine (H-rGO) as reducing agent, as well as carbonaceous materials including carbon

nanofibers (CNFs) and graphitized mesoporous carbon (gCMK-3) were synthesized, characterized and tested toward OER/ORR and compared to commercial carbon black (CB) and graphite (G). Additionally, the corrosion resistance properties of the electrocatalysts under strongly oxidizing conditions have been investigated. Physicochemical characterization was conducted by X-ray diffraction (XRD), X-ray photoelectron spectroscopy (XPS), elemental analysis and Raman spectroscopy. The catalytic performance of the catalysts toward ORR and OER in alkaline medium (0.1 M NaOH) was carried out by the rotating ring-disk electrode (RRDE) technique.

## 2. Experimental

### 2.1. Materials

Sulfuric acid (95-97%; Merck), sodium hydroxide (99.99%; Sigma-Aldrich), potassium permanganate (>99.8%; Sigma-Aldrich), thiourea (>99%; Fluka), hydrazine (>99%; Sigma-Aldrich), tetraethyl orthosilicate (>98.0%; Sigma-Aldrich), Pluronic P123 Sigma-Aldrich), Vulcan XC-72R (Cabot), graphite (>99.8%; Sigma-Aldrich), hydrogen peroxide (30% v/v; Foret) and water (18.2 M  $\Omega\cdot\text{cm}$ ; Milli-Q, Millipore) were purchased and then used for the synthesis of the graphene materials and the preparation of the electrolyte solutions.

### 2.2. Synthesis of Graphene Oxide (GO) and Reduced Graphene Oxide (H-rGO)

GO was prepared by following a modified Hummers method [22]; 1 g of the graphite powder was added to 30 mL of concentrated  $\text{H}_2\text{SO}_4$  cooled in an ice bath. Then, 3.5 g of  $\text{KMnO}_4$  was slowly introduced while being stirred and cooled continuously. After removal from the ice bath, the mixture was diluted with Milli-Q water and sonicated for 1 h at 35 °C. Then, the solution was heated up to 95–98 °C over 30 min. Next, 200 mL of ultrapure water was gradually introduced, followed by 1.25 mL of 30% v/v  $\text{H}_2\text{O}_2$ , and the stirring was maintained for 30 min. Finally, the dispersion was centrifuged with Milli-Q water until a pH of 7 was achieved in the supernatant liquid. The resultant GO material was dried using an oven at 60 °C.

In order to produce reduced graphene oxide (H-rGO), an adequate amount of hydrazine (1 $\mu\text{L}$  of hydrazine by 3 mg GO) was mixed with a GO aqueous dispersion (3 mg GO

$\text{mL}^{-1}$ ) using an ultrasound bath. Then, this dispersion was kept in refluxing during 12 h. Afterwards, the resultant material (H-rGO) was washed using abundant Milli-Q water (about 3 L) and then transferred to an oven at 60 °C for 24 h to obtain a reduced GO powder. The percentage yield was close to 90 %.

### 2.3. *Synthesis of carbon nanofibers (CNFs)*

Carbon nanofibers (CNFs) were grown by methane decomposition over a Ni:Cu: $\text{Al}_2\text{O}_3$  (molar ratio 78:6:16) catalyst. The reaction was carried out in a pure methane flow at 700 °C during 10 h as described in [23]. These growth conditions of CNFs result in a fishbone type structure, carbon stacked layers at about 20° with respect to growth axis, with average fiber diameter of about 50 nm, according to a previous work [24].

### 2.4. *Synthesis of mesoporous carbon (gCMK-3)*

Ordered mesoporous carbon (gCMK-3) was prepared by incipient wetness impregnation of Santa Barbara Amorphous-15 (SBA-15) silica with furan resin (Huttenes-Albertus) as carbon precursor. Impregnated silica was carbonized in a pure nitrogen flow (flow rate = 100  $\text{cm}^3 \text{ min}^{-1}$ ) at 700 °C during 2 h. The obtained silica-carbon composite was washed with HF (40%) for 24 h to remove SBA-15 silica and then washed with distilled water, as described previously in [25]. Finally, the carbon material was subjected to heat treatment at 1500 °C in order to increase its crystalline grade and, therefore, its electrical conductivity. This treatment was carried out in a graphite electrical furnace for 1 h under argon flow, using a heating rate of 10 °C  $\text{min}^{-1}$ .

### 2.4. *Physicochemical Characterization*

XRD powder spectra were acquired from a X’Pert PRO X-ray diffractometer (PANalytical) to determine the crystal structure. Measurements were obtained using the CuK $\alpha$  radiation ( $\lambda = 1.5405 \text{ \AA}$ ) and the X’pert high score plus diffraction software, and  $2\theta$  data were collected from 20° to 100° with a scanning rate of 0.04°  $\text{s}^{-1}$ . Crystalline phases were identified by comparing the experimental diffraction patterns with the Joint Committee on Powder Diffraction Standards (JCPDS).

Elemental analysis with an experimental error close to 0.04% was performed using an Elemental Analyzer CNHS FLASH EA 1112 (Thermo Scientific).

Raman spectra were collected using a RENISHAW confocal Raman microscope, model inVia (RENISHAW), with a green laser ( $\lambda = 532$  nm) in the 100 to  $3200\text{ cm}^{-1}$  range.

Chemical composition of the catalysts was determined by energy dispersive X-ray analysis (EDX, Oxford 6699 ATW), and X-ray photoelectron spectroscopy (XPS) data were obtained with a SPECS GmbH customized system (SPECS™) for surface analysis, equipped with a non-monochromatic X-ray source XR 50 and a hemispherical energy analyzer (PHOIBOS 1509MCD).

Photoelectrons were excited by using MgK $\alpha$  line (1253.6 eV) operating at 200 W/12 kV. Powder samples were attached onto a Cu foil and were placed first in the pre-treatment chamber at room temperature for several hours, before being transferred to the analysis chamber. The XPS data were signal averaged for a large enough number of scans to get a good signal/noise ratio, at increments of 0.1 eV and fixed pass energy of 25 eV. High-resolution spectra were obtained by curve fitting synthetic peak components, using the software XPSpeak41. The raw data were used with no preliminary smoothing. Symmetric Gaussian—Lorentzian product functions, after the elimination of background noise upon use of Shirley-type curves, were employed to approximate the line shapes of the fitting components. Binding energies were calibrated relative to the C 1s peak from the graphitic carbon at 284.6 eV.

## *2.5. Electrochemical Characterization*

All measurements were carried out in an electrochemical cell at room temperature controlled by an Autolab PGSTAT302N potentiostat-galvanostat. A carbon rod was used as a counter electrode, while the reference electrode was a reversible hydrogen electrode (RHE) in the supporting electrolyte (0.1 M NaOH). All potentials are referred to this electrode. A rotating ring-disk electrode (RRDE) composed of Pt ring and glassy carbon disk (geometrical area =  $0.196\text{ cm}^2$ ) was used. The working electrode consisted of a certain amount of the catalyst (0.077 mg) deposited as a thin layer over the glassy carbon disk. The suspension was prepared by stirring 2 mg of catalyst with 15  $\mu\text{L}$  of Nafion® (5%, Sigma–Aldrich) and 0.5 mL of water (Milli-Q, Millipore). Ar (99.999%,

Air Liquide) was used to deoxygenate all solutions and O<sub>2</sub> (99.995%, Air Liquide) for those measurements related to ORR.

For the ORR experiments, O<sub>2</sub> was bubbled during 30 min before and during all the measurements to maintain the electrolyte saturated. Polarization measurements were recorded between 1.0 and 0.2 V at rotating speeds of 400, 600, 900, 1600 and 2500 rpm. In these experiments, the working electrode was introduced into the electrolyte at controlled potential of 1.0 V. Then, the applied potential was held at 1.0 V during 1 min, and after that, the linear sweep voltammetry (LSV) was initiated in the negative direction at scan rate of 0.002 V s<sup>-1</sup>. In order to detect hydrogen peroxide formation, the ring potential was maintained constant at 1.2 V during the ORR. For the OER, a LSV was recorded between 0.1 and 2.3 V at a scan rate of 0.01 V s<sup>-1</sup> and a fix rotating rate of 1600 rpm, meanwhile a constant potential of 0.4 V was applied at the ring electrode. The latter was employed in order to distinguish the OER from other anodic reactions, e.g. carbon dioxide formation from catalyst support corrosion.

### 3. Results and discussion

#### 3.1. Physicochemical Characterization

Figure 1 displays the XRD patterns obtained for the different carbon materials. Graphite reveals a sharp diffraction peak at 26.5°, which is related to the C(002) plane, and a small diffraction peak at 54.3° associated to the (004) facet. The GO formation from the oxidation of graphite is detected by the broad diffraction peak at 10.7°, which is related to the (001) diffraction plane and by the absence of the diffraction peaks associated to graphite. The last is caused by the growth of oxygen functional groups (OFGs) between the graphitic layers, which caused an expansion of the C–C interplanar spacing from 0.34 to 0.84 nm (Table 1), and therefore, a weakening of the respective chemical bonds of graphite [22]. H-rGO develops broad diffraction peaks at ca. 15.3° and 23.8°, which suggest that OFGs in the interstitial graphitic spaces were incompletely reduced and that the C–C lattice of graphite was partially restored. Additionally, a sharp peak at 42.8° is discerned at H-rGO, which is related to the (100) facet. gCMK-3 material also shows the (002) reflection in its XRD patterns. However, it is broader and shifted to lower angles (24.6°) in comparison to graphite, which is indicative of its more amorphous character. This broadening can also be explained in terms of crystallite size, as discussed below. On

the other hand, CNF shows three peaks at  $26.3^\circ$ ,  $42.8^\circ$  and  $54.2^\circ$  that are attributed to the (002), (100) and (004) reflections of graphitic carbon. In addition, CNF exhibits two other peaks at  $44.3^\circ$  and  $51.7^\circ$ , associated to the (111) and (200) reflections of nickel, which was used as catalyst during the synthetic procedure [23,26]. It is important to note that the small amount of nickel remains only inside the CNF [23,26].

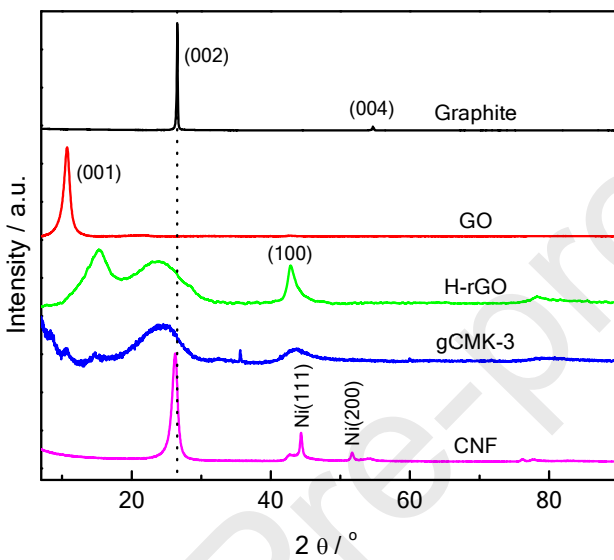


**Figure 1.** X-ray diffraction (XRD) patterns for all studied materials.

Crystallite size for all employed catalysts was calculated by the Scherrer equation (Table 1). H-rGO material revealed a crystallite size ( $L_c$ ) smaller than that of graphite and GO, which is in agreement with the number of graphene layers ( $n_l$ ). In this sense,  $n_l$  was estimated from the ratio of the  $L_c$  and the interplanar spacing ( $d_{hkl}$ ), and as expected, graphite showed the highest  $n_l$  and  $L_c$ . Table 1 clearly depicts that the oxidation process (GO formation) produces OFGs (C/O ratio decreases), and therefore, an increment of the interplanar spacing between graphene layers ( $d_{001} = 0.83$  nm) and a reduction of  $L_c$  and  $n_l$  is discerned. On the other hand, the reduction process (H-rGO formation) produces a further diminution of  $d_{hkl}$ ,  $L_c$  and  $n_l$  parameters. Interestingly, gCMK-3 and CNF reveal similar  $d_{002}$  than H-rGO and Graphite, respectively. A crystallite size of 10.41 nm was calculated for CNFs compared with the 1.12 nm for gCMK-3, indicating the higher graphitization degree of the former.

All features observed by X-ray diffraction (XRD) were in agreement with those results achieved by elemental analysis (Table 1). Indeed, an increment of oxygen concentration (decrease of C/O ratio) was observed after the chemical oxidation process of graphite to produce GO, which diminishes after the reduction step to produce H-rGO. Hydrazine is a weak reducing agent, which is confirmed by the small C/O ratio of H-rGO.. Nevertheless, hydrazine is effective to introduce nitrogen species into the graphenic network (1.8 wt%). On the other hand, gCMK-3 depicts de highest C/O composition ratio, meanwhile CNF reveals similar ratio than Graphite.

**Table 1. Physicochemical parameters obtained by XRD<sup>a</sup>, Raman<sup>b</sup> and Elemental Analysis<sup>c</sup> for all studied materials.**

Materials	<sup>a</sup> d <sub>002</sub> (nm)	<sup>a</sup> L <sub>c</sub> (nm)	<sup>a</sup> n <sub>l</sub>	<sup>b</sup> I <sub>D</sub> /I <sub>G</sub>	<sup>b</sup> L <sub>a</sub> (nm)	<sup>c</sup> C (wt%)	<sup>c</sup> O (wt%)	<sup>c</sup> C/O (wt%)	<sup>c</sup> N (wt%)
Graphite	0.34	66.35	195	0.23	83.6	80.0	20.0	4.0	---
GO	0.83(d <sub>001</sub> )	8.05	10	0.88	21.8	49.0	51.0	1.0	---
H-rGO	0.38	1.41	4	0.94	20.5	64.0	34.6	1.8	1.4
gCMK-3	0.38	1.12	---	1.15	16.7	92.0	8.0	11.5	---
CNF	0.35	10.41	---	1.27	15.1	80.0	20.0	4.0	---

d<sub>002</sub>: interplanar C-C distance, L<sub>c</sub>: crystallite size, L<sub>a</sub>: basal plane size, n<sub>l</sub>: number of graphenic layers

Raman spectroscopy was employed to measure the disorder degree, defect density and crystallinity of carbon-based materials [27]. Figure 2 depicts the Raman spectra for all studied materials, in which four contributions are clearly discerned. The peaks at ca. 1360 cm<sup>-1</sup> (D) and 1580 cm<sup>-1</sup> (G) are correlated to sp<sup>3</sup> carbon domains and to sp<sup>2</sup> bonds into the graphitic grid, respectively [27]. Both signals have their corresponding overtones between 2500 and 3000 cm<sup>-1</sup>, respectively [27]. The intensity ratio of D and G peaks (Table 1) are usually employed as a measurement of the disorder degree, graphitization and crystallinity of the synthesized materials [28,29]. For instance, GO reveals broader D and G peaks, as well as a more intense D peak ( $I_D/I_G = 0.88$ ) than graphite ( $I_D/I_G = 0.23$ ), which shows a prominent G peak in agreement with the high size of the in-plane sp<sup>2</sup> domains. H-rGO develops the typical Raman spectra for heteroatom-doped rGO as a result of carbon hybridization by N–C bond formation and/or for some structural disorder

(impurities, edges, finite size effects, etc.) that breaks the translational symmetry [30]. The lowest  $L_a$  of CNF is associated to the limited dimension of stacked graphene layers conforming the fiber structure, thus contributing to larger edge-to-basal atoms than other graphitic materials and higher  $I_D/I_G$  as a result [24]. Then,  $I_D/I_G$  values increases in the following order: Graphite << GO < H-rGO < gCMK3 < CNF. It is noticeable the sharp band developed by CNF, which may be ascribed to the big crystallite size and to a preferential orientation of the nanofibers.

Graphitic materials can also be characterized through their structural parameters that depend on the crystallographic size in parallel and perpendicular directions to their planes, that is,  $L_a$  and  $L_c$  (see Table 1). The  $L_c$  value is obtained by the Scherrer equation from XRD data, while  $L_a$  is estimated from the  $I_D/I_G$  ratio from Raman through the empirical equation developed by Knight and White [31,32]. Figure 3 displays a linear correlation between  $I_D/I_G$  and the inverse of  $L_a$  for all studied catalysts. A close inspection of this plot suggests that  $L_a$  not only decreases with Graphite oxidation, but also with the strength of the doping agent (as we described above hydrazine is a weak reducing agent) and the structural morphology of the carbonaceous material.

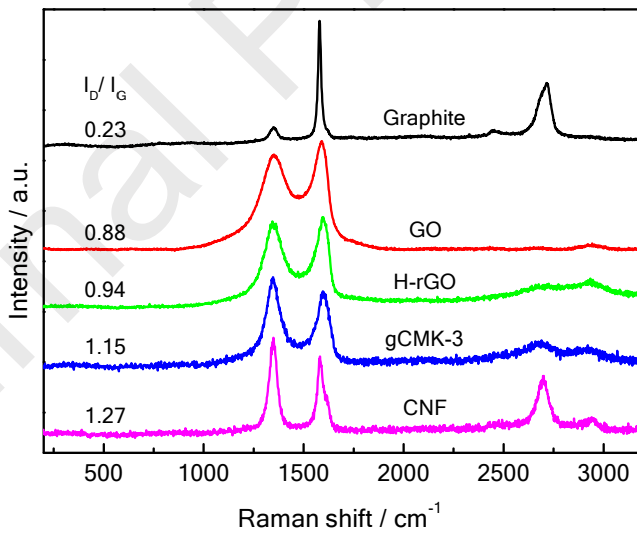


**Figure 2.** Raman spectra for all studied materials.

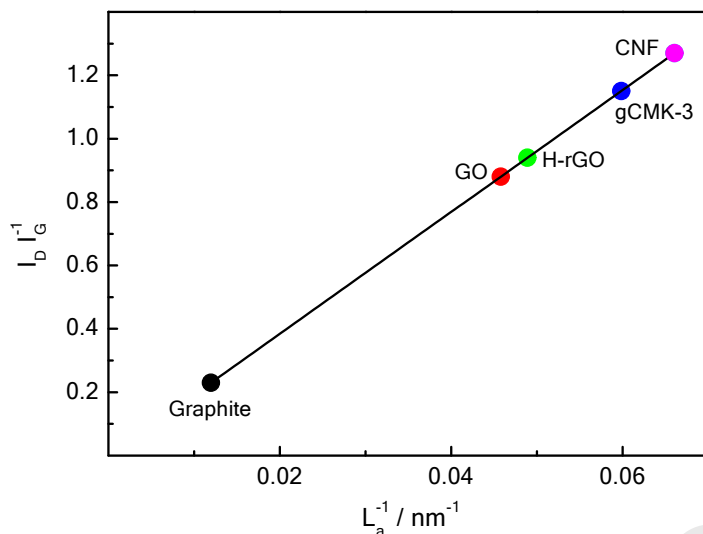


**Figure 3.** Plot of  $I_D/I_G$  ratio vs.  $1/L_a$  for all studied materials.

X-ray photoelectron spectroscopy (XPS) was carried out to identify and quantify the surface composition and the chemical state of the elements. Deconvoluted spectra for C and O are presented in Figure 4.

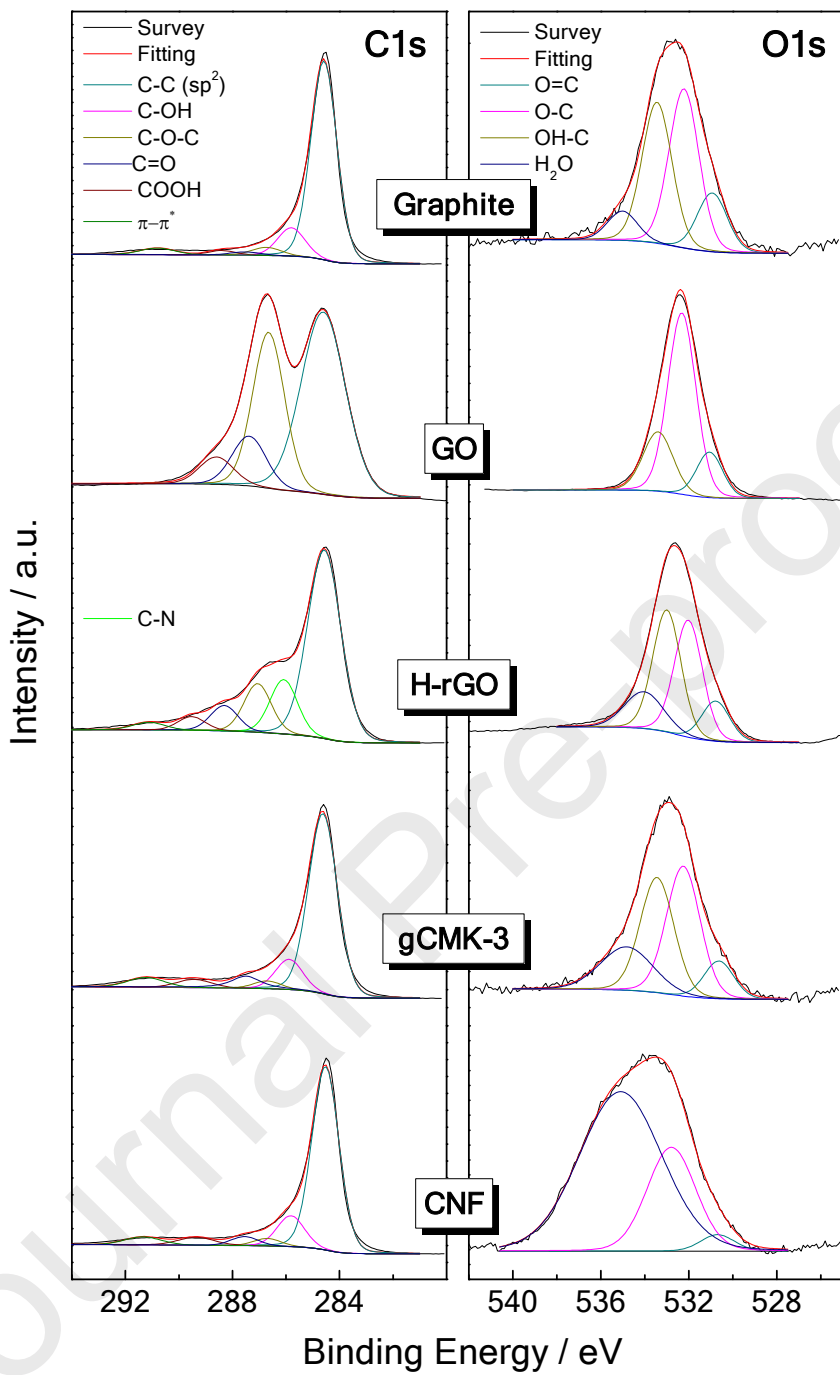


**Figure 4.** C 1s (left panels) and O 1s (right panels) XPS spectra for all studied materials.

The C 1s signal provides detailed information about the presence of oxygen and nitrogen species bonded to carbon atoms (left panels of Figure 4). As can be seen, the carbon signal is mainly composed by graphitic carbon ( $sp^2$ ), followed by different oxygenated species

at higher binding energy values, such as C–OH, C–O–C, C=O and carboxylic bonds [33]. In addition to these signals, H-rGO reveals an additional component at ca. 286.1 eV (green line) ascribed to nitrogen species bonded to carbon atoms. Also, a small but visible signal at ca. 289.0 eV ascribed to a  $\pi-\pi^*$  shake-up satellite is discerned [34]. It is noticeable the high amount of C–O–C species produced after the Graphite oxidation procedure, which considerably remains after the soft reduction process by hydrazine that is in perfect agreement with the observed by other techniques and described above.

Interestingly, the O1s signal (right panels of Figure 4) reveals different surface oxygenated species, which strongly depend on the carbonaceous material [33]. Remarkably, intercalated water (blue line) signal is intense at CNF, but is not perceived at GO. In agreement with the C1s signal, GO is mainly composed by C–O species (pink line).

Transmission electron microscopy (TEM) and scanning electron microscopy (SEM) images, as well as, BET analysis for all studied materials are included in the supporting information (SI). All results depicted in the SI agree to the physicochemical characterization described above. Interestingly, the specific surface area increases in the subsequent order: Graphite < GO < CNFs < H-rGO < gCMK-3.

All the described morphological and chemical changes modify relevant physicochemical properties with profound impacts on electrochemical reactions such as the ORR and OER. By affecting the electrical conductivity (higher in basal planes than in edge planes), electron transfer (higher in edge planes than in basal planes), different adsorption and bond cleavage of O<sub>2</sub> (tuned by N insertion into the graphene network), diverse electronic density of states near the Fermi level: the overall catalytic performance (activity and stability) of carbon-based materials during both reactions (ORR/OER) will be altered [30,35].

### *3.2. Electrochemical Characterization*

It is well-known that the ORR and the OER depend on several parameters, such as the catalyst composition (morphological and electronic factors), the applied potential, the nature of the ions dissolved in the electrolyte and the pH of the media [36–41]. In order to study the catalytic performance and discern the ORR pathway for the different catalysts, the rotating ring-disk electrode (RRDE) technique was applied (Figure 5). The

middle panel shows the ORR polarization curves recorded at  $0.002 \text{ V s}^{-1}$  in  $0.1 \text{ M NaOH}$ , meanwhile the top panel depicts the signal acquired with the ring electrode at  $1.2 \text{ V}$  that detects the peroxide production (incomplete ORR pathway).

Graphite developed the worst catalytic activity toward the ORR, which may have been ascribed to the low density of edge planes (i.e. high  $L_c$  value) and long basal plane size ( $L_a$ ) and to the absence of doping and impurities. In other words, the ORR strongly increased for materials with short  $L_a$  (and high density of edge planes,  $L_c$ ) and with the insertion of nitrogen into the graphenic structure. Thus, H-rGO revealed the lowest onset potential at ca.  $0.91 \text{ V}$  for the ORR. The latter was promoted by the high oxygen loading and by N-doping, which creates a charge polarization of the N–C bond, and therefore the adsorption ( $\text{O}_{2(\text{ads})}$ ) and dissociation (O–O bond cleavage) of  $\text{O}_2$  were facilitated [30]. In addition, nickel species into the CNF may promote the ORR only by electronic effects due to is embedded in the carbon structure [23,26]. Then, the catalytic activity toward the ORR at high pH increases in the following order: Graphene < gCMK-3 < CNF < H-rGO.

In order to evaluate the final product of the ORR, and consequently, the mechanism of the reaction, the peroxide formation was followed at the ring electrode (top panel of Figure 5), and the number of electrons transferred ( $n$ ) was calculated (bottom panel of Figure 5) by the equation [42]:

$$n = 4i_D/(i_D + i_R/N) \quad (1)$$

where  $N$  is the current collection efficiency of the ring (0.22), and  $i_D$  and  $i_R$  are the disk and ring currents, respectively. A close inspection of the bottom panel of the figure indicates almost a full molecular oxygen ( $\text{O}_2$ ) conversion to water (four-electron pathway) on CNF and H-rGO materials at  $E < 0.80 \text{ V}$ . Indeed, Graphite and gCMK-3 not only revealed a higher overpotential for the ORR, but also a minor energy conversion efficiency, that is, half of the reactant produced water (four electrons) and the other half-generated peroxide (two-electron pathway). Furthermore, it is well recognized that  $\text{H}_2\text{O}_2$  accelerates the degradation of the polymeric membrane electrolyte membrane in fuel cells (FCs). Hence, CNF and H-rGO appear as suitable catalysts to be employed as cathode due to not only their high catalytic activity but also that can increase the durability of FCs and URFCs.

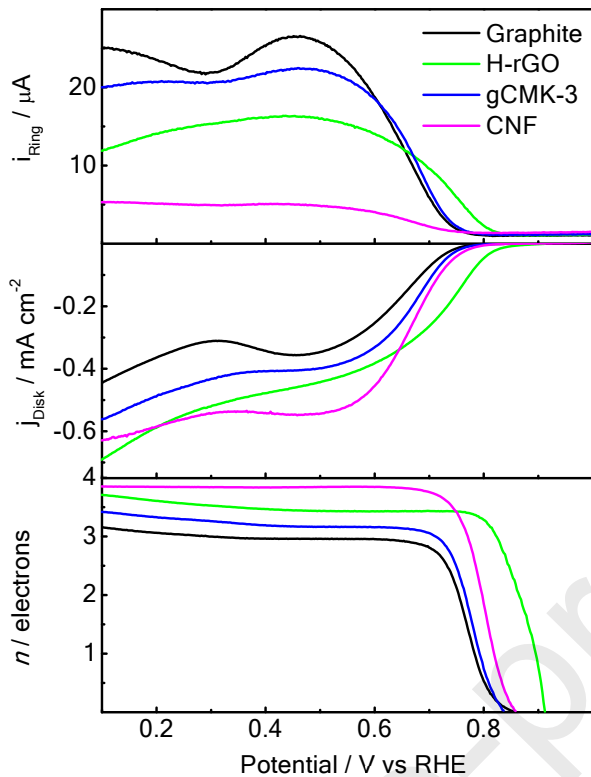


**Figure 5.** Steady-state polarization curves for  $\text{O}_2$  reduction at 1600 rpm in 0.1 M NaOH at 25 °C for all employed electrocatalysts (middle panel); faradaic currents developed at 1.2 V at the Pt ring electrode (top panel); number of electrons transferred ( $n$ ) during the oxygen reduction reaction (ORR; bottom panel). Sweep rate of 0.002 V s<sup>-1</sup>.

Figure 6 shows the OER polarization curves for all catalysts (bottom panel) and the signal acquired at the ring electrode (upper panel). H-rGO reveals the most negative onset potential ( $\approx 1.15$  V) and a small but visible anodic current at more positive potentials. gCMK-3, CNF and Graphite show an onset potential at ca. 1.3, 1.5 and 1.6 V, respectively. Additionally, the anodic current rises at higher overpotentials on these materials. In order to confirm which anodic contribution is associated with the OER, the ring electrode was held at 0.4 V. Therefore, molecular oxygen produced at the working electrode arrives to the ring and it is reduced to water, and consequently the OER can be discerned. Negligible cathodic currents are observed at the ring for g-CMK-3 and H-rGO catalysts, which suggest that both materials are not producing molecular oxygen but are corroded at this potential region. On the other hand, CNF and Graphite developed cathodic currents at the ring electrode, and therefore, are active materials for the OER in

the potential range under study. Thus, short interplanar C-C distance and low specific surface area appear as the main factors to promote the OER. In this sense, materials containing high amount of oxide species (low C/O ratio), functional groups and doping reveal longer interplanar C-C distance and higher specific surface area and therefore low activity toward the OER.

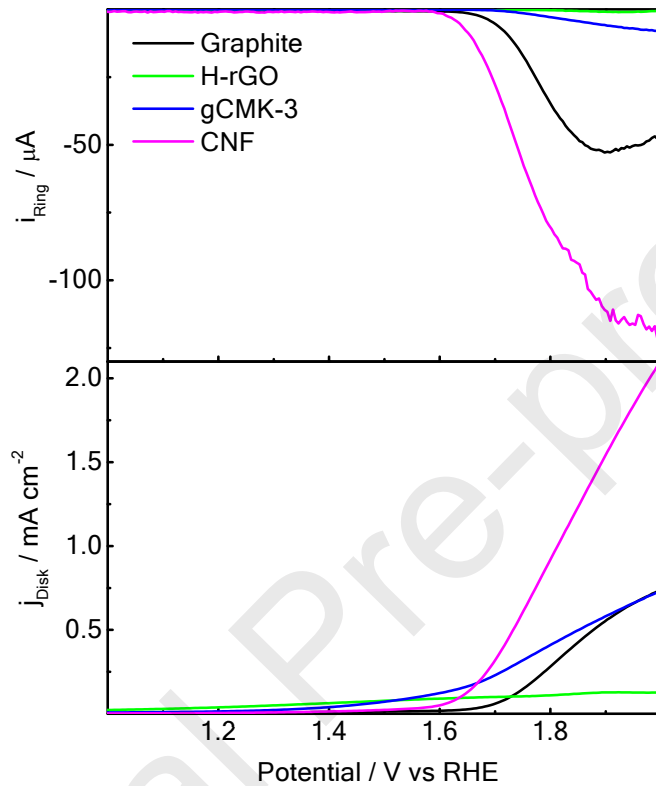


**Figure 6.** Steady-state polarization curves recorded at  $0.01 \text{ V s}^{-1}$  and 1600 rpm in 0.1 M NaOH at  $25^\circ\text{C}$  for all employed electrocatalysts (bottom panel); faradaic currents developed at 0.4 V at the Pt ring electrode (top panel).

A simple equation to estimate the amount of oxygen produced by the catalysts can be employed, assuming that only the OER ( $I_{\text{O}_2}$ ) and the corrosion ( $I_{\text{CO}_2}$ ) of the materials happen at the disk electrode ( $I_{\text{Disk}}$ ):

$$I_{\text{Disk}} = I_{\text{O}_2} + I_{\text{CO}_2} \quad (2)$$

On the other hand, the reduction of oxygen is the only reaction detected at the ring electrode ( $I_{Ring}$ ). Then, the correlation between  $I_{Ring}$  and  $I_{O_2}$  can be easily reached employing the collection efficiency ( $N = 0.22$ ) of the RRDE:

$$I_{O_2} = I_{Ring} / N \quad (3)$$

Then, the molar percentage of  $O_2$  ( $\chi_{O_2} \cdot 100$ ) produced at the carbon-based catalyst can be acquired from the subsequent equation:

$$\chi_{O_2} \cdot 100 = \frac{I_{O_2}}{I_{O_2} + I_{CO_2}} \cdot 100 \quad (4)$$

Finally, replacing equations (3) and (2) and rearranging terms:

$$\chi_{O_2} \cdot 100 = \frac{I_{Ring}}{I_{Disk} N} \cdot 100 \quad (5)$$

Figure 7 shows the  $\chi_{O_2} \cdot 100$  produced for all carbon-based catalysts in alkaline medium. Noticeable is the zero production of oxygen by the graphenic catalyst (H-rGO). In addition, from this figure becomes clear that the onset potential and the catalytic activity toward the OER increase in the following order: CNF < Graphite << gCMK-3. However, CNF corrodes at smaller overpotentials than Graphite. In agreement with the described above, a short interplanar C-C distance with a rigid carbon structure appear as the main reasons for the high catalytic activity and stability developed by CNF and Graphite catalysts. Additionally, the presence of nickel into the CNF structure may slightly enhance the activity toward the OER.

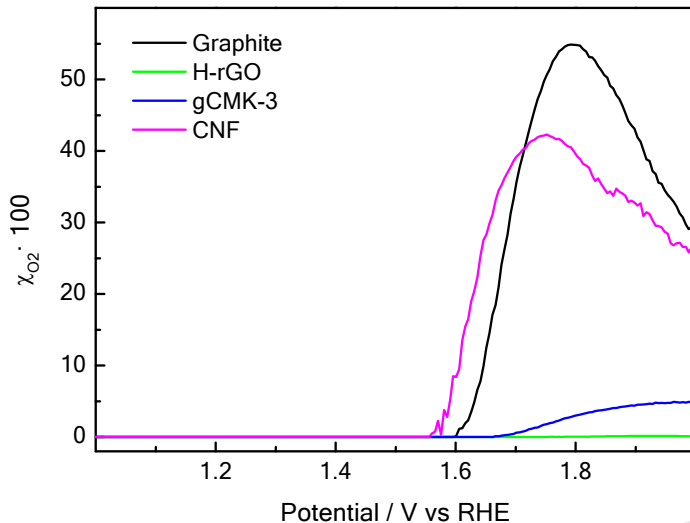


**Figure 7.** Percentage of molecular oxygen produced for all employed electrocatalysts in 0.1 M NaOH.

In summary, CNF is the most active catalyst toward the OER and shows good catalytic activity toward the ORR. Consequently, CNF appears as the most suitable catalyst to be employed as bifunctional oxygen electrode in URFC. The research opens different avenues where CNFs can be used in combination with other material to develop durable catalysts for practical URFC use.

#### 4. Conclusions

The bifunctional oxygen electrode plays a central role in developing URFC. The low catalytic performance and the high cost of platinum group metals (PGM) usually employed as bifunctional catalysts can be dealt with novel carbonaceous materials. With this end in view, the properties of Graphite, H-rGO, gCMK-3 and CNFs materials as bi-operational oxygen electrode catalysts were investigated. It was observed that the ORR and the OER strongly depend on the basal plane size, the density of edge planes, the interplanar C-C distance and the oxygen as well as the nitrogen content into the graphenic structure. Results reveal the best performance toward the ORR and the OER for CNFs material, in addition to the best compromise between catalytic activity and stability. On the other hand, H-rGO presents the highest catalytic activity toward the ORR, but it is not active for the OER. gCMK-3 appears to be the catalyst with the worst performance and

stability, while Graphite shows acceptable activity towards both reactions. Finally, main conclusion reveals that CNFs can act as a feasible catalyst for URFC applications.

## Acknowledgements

The Spanish Ministry of Economy and Competitiveness (MINECO) has supported this work under project ENE2017-83976-C2-2-R (co-funded by FEDER). L.M.R. thanks the ACIISI for his PhD fellowships and G.G. acknowledges the Viera y Clavijo program (ACIISI and ULL) for financial support. Authors would like to acknowledge the use of SEGAI—ULL facilities and Victor Lavin for Raman experiments.

## References

- [1] Roca-Ayats M, García G, Galante JL, Peña MA, Martínez-Huerta M V. Electrocatalytic stability of Ti based-supported Pt<sub>3</sub>Ir nanoparticles for unitized regenerative fuel cells. *Int J Hydrogen Energy* 2014;39:5477–84.  
doi:10.1016/j.ijhydene.2013.12.187.
- [2] Edwards PP, Kuznetsov VL, David WIF, Brandon NP. Hydrogen and fuel cells: Towards a sustainable energy future. *Energy Policy* 2008.  
doi:10.1016/j.enpol.2008.09.036.
- [3] European Commission. Hydrogen Energy and Fuel Cells. 2003. doi:92-894-5589-6.
- [4] Dutta K, Rana D, Han HS, Kundu PP. Unitized Regenerative Fuel Cells: A Review on Developed Catalyst Systems and Bipolar Plates. *Fuel Cells* 2017;17:736-751.  
doi:10.1002/fuce.201700018.
- [5] Wang Y, Leung DYC, Xuan J, Wang H. A review on unitized regenerative fuel cell technologies, part-A: Unitized regenerative proton exchange membrane fuel cells. *Renewable and Sustainable Energy Reviews* 2016;65:961-977. doi:10.1016/j.rser.2016.07.046
- [6] Millet P, Ngameni R, Grigoriev SA, Fateev VN. Scientific and engineering issues related to PEM technology: Water electrolyzers, fuel cells and unitized regenerative systems. *Int J Hydrogen Energy* 2011.  
doi:10.1016/j.ijhydene.2010.06.106.
- [7] García G, Roca-Ayats M, Lillo A, Galante JL, Peña MA, Martínez-Huerta M V. Catalyst support effects at the oxygen electrode of unitized regenerative fuel

- cells. *Catal Today* 2013;210:67–74. doi:10.1016/j.cattod.2013.02.003.
- [8] Park S, Shao Y, Liu J, Wang Y. Oxygen electrocatalysts for water electrolyzers and reversible fuel cells: Status and perspective. *Energy Environ Sci* 2012. doi:10.1039/c2ee22554a.
- [9] Chen JJ, Xu DG. Recent Development and Applications in Electrodes for URFC. *Int Lett Chem Phys Astron* 2015. doi:10.18052/www.scipress.com/ilcpa.47.165.
- [10] Pettersson J, Ramsey B, Harrison D. A review of the latest developments in electrodes for unitised regenerative polymer electrolyte fuel cells. *J Power Sources* 2006;157:28–34. doi:10.1016/j.jpowsour.2006.01.059.
- [11] Cruz JC, Baglio V, Siracusano S, Ornelas R, Arriaga LG, Antonucci V, Aricò AS. Nanosized Pt/IrO<sub>2</sub> electrocatalyst prepared by modified polyol method for application as dual function oxygen electrode in unitized regenerative fuel cells. *International Journal of Hydrogen Energy* 2012;37 (7):5508-5517. doi: 10.1016/j.ijhydene.2011.12.153.
- [12] Altmann S, Kaz T, Friedrich KA. Bifunctional electrodes for unitised regenerative fuel cells. *Electrochimica Acta* 2011;56 (11):4287-4293. doi: 10.1016/j.electacta.2011.01.077.
- [13] Katsounaros I, Cherevko S, Zeradjanin AR, Mayrhofer KJJ. Oxygen electrochemistry as a cornerstone for sustainable energy conversion. *Angew Chemie - Int Ed* 2014;53:102–21. doi:10.1002/anie.201306588.
- [14] Alegre C, Busacca C, Di Blasi A, Di Blasi O, Aricò AS, Antonucci V, Modica E, Baglio V. Electrospun carbon nanofibers loaded with spinel-type cobalt oxide as bifunctional catalysts for enhanced oxygen electrocatalysis. *Journal of Energy Storage* 2019;23:269-277. doi: 10.1016/j.est.2019.04.001.
- [15] Wang YJ, Fang B, Wang X, Ignaszak A, Liu Y, Li A, Zhang L, Zhang J. Recent advancements in the development of bifunctional electrocatalysts for oxygen electrodes in unitized regenerative fuel cells (URFCs). *Progress in Materials Science* 2018;98:108-167. doi: 10.1016/j.pmatsci.2018.06.001.
- [16] Alegre C, Modica E, Di Blasi A, Di Blasi O, Busacca C, Ferraro M, Aricò AS, Antonucci V, Baglio V. NiCo-loaded carbon nanofibers obtained by electrospinning: Bifunctional behavior as air electrodes. *Renewable Energy* 2018; 125:250-259. doi: 10.1016/j.renene.2018.02.089.
- [17] da Silva GC, Mayrhofer KJJ, Ticianelli EA, Cherevko S. Dissolution stability: The major challenge in the regenerative fuel cells bifunctional catalysis. *Journal of the*

- Electrochemical Society 2018;165(16):F1376-F1384. doi: 10.1149/2.1201816jes
- [18] Alegre C, Modica E, Aricò AS, Baglio V. Bifunctional oxygen electrode based on a perovskite/carbon composite for electrochemical devices. *Journal of Electroanalytical Chemistry* 2018;808:412-419. doi: 10.1016/j.jelechem.2017.06.023.
- [19] Alegre C, Busacca C, Di Blasi O, Antonucci V, Aricò AS, Di Blasi A, Baglio V. A combination of CoO and Co nanoparticles supported on electrospun carbon nanofibers as highly stable air electrodes. *Journal of Power Sources* 2017;364:101-109. doi: 10.1016/j.jpowsour.2017.08.007.
- [20] Sadhasivam T, Roh SH, Kim TH, Park KW, Jung HY. Graphitized carbon as an efficient mesoporous layer for unitized regenerative fuel cells. *International Journal of Hydrogen Energy* 2016;41(40):18226-18230. doi: 10.1016/j.ijhydene.2016.08.092.
- [21] Su Y, Zhu Y, Jiang H, Shen J, Yang X, Zou W, Chen J, Li C. Cobalt nanoparticles embedded in N-doped carbon as an efficient bifunctional electrocatalyst for oxygen reduction and evolution reactions. *Nanoscale* 2014;6(24): 15080-15089. doi: 10.1039/C4NR04357J
- [22] Rivera LM, Fajardo S, Arévalo M del C, García G, Pastor E. S- and N-Doped Graphene Nanomaterials for the Oxygen Reduction Reaction. *Catalysts* 2017;7.
- [23] Calvillo L, Lázaro MJ, Suelves I, Echegoyen Y, Bordejé EG, Moliner R. Study of the Surface Chemistry of Modified Carbon Nanofibers by Oxidation Treatments in Liquid Phase. *J Nanosci Nanotechnol* 2009. doi:10.1166/jnn.2009.m26.
- [24] Sebastián D, Ruiz AG, Suelves I, Moliner R, Lázaro MJ. On the importance of the structure in the electrical conductivity of fishbone carbon nanofibers. *J Mater Sci* 2013;48: 1423-1435. doi: 10.1007/s10853-012-6893-1.
- [25] Calvillo L, Celorio V, Moliner R, Cabot PL, Esparbé I, Lázaro MJ. Control of textural properties of ordered mesoporous materials. *Microporous Mesoporous Mater* 2008. doi:10.1016/j.micromeso.2008.04.015.
- [26] Calvillo L, Celorio V, Moliner R, Garcia AB, Caméan I, Lazaro MJ. Comparative study of Pt catalysts supported on different high conductive carbon materials for methanol and ethanol oxidation. *Electrochim Acta* 2013;102:19–27. doi:10.1016/j.electacta.2013.03.192.
- [27] Botas C, Álvarez P, Blanco C, Santamaría R, Granda M, Gutiérrez MD, et al.

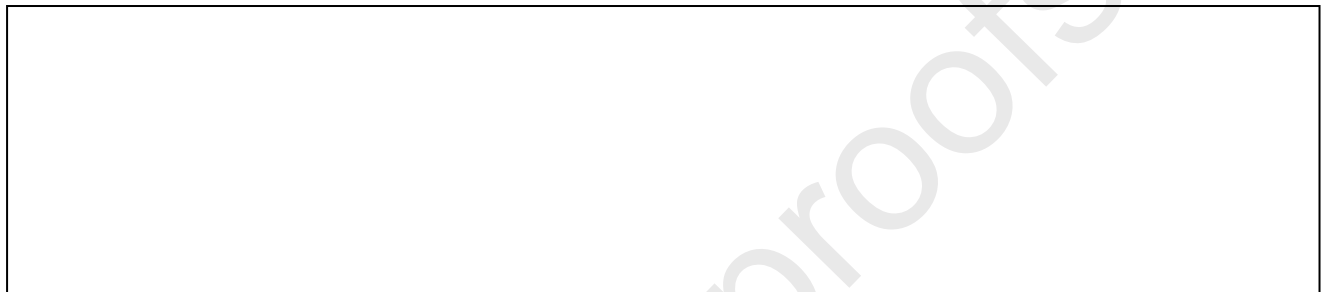
- Critical temperatures in the synthesis of graphene-like materials by thermal exfoliation-reduction of graphite oxide. *Carbon N Y* 2013.  
doi:10.1016/j.carbon.2012.09.059.
- [28] Saner B, Dinç F, Yürüm Y. Utilization of multiple graphene nanosheets in fuel cells: 2. the effect of oxidation process on the characteristics of graphene nanosheets. *Fuel* 2011. doi:10.1016/j.fuel.2011.03.040.
- [29] Kiciński W, Szala M, Bystrzejewski M. Sulfur-doped porous carbons: Synthesis and applications. *Carbon N Y* 2014. doi:10.1016/j.carbon.2013.11.004.
- [30] Rivera LMLM, Fajardo S, Arévalo MCM del C, García G, Pastor E. S- and N-Doped Graphene Nanomaterials for the Oxygen Reduction Reaction. *Catalysts* 2017;7:278. doi:10.3390/catal7090278.
- [31] Cançado LG, Takai K, Enoki T, Endo M, Kim YA, Mizusaki H, et al. General equation for the determination of the crystallite size La of nanographite by Raman spectroscopy. *Appl Phys Lett* 2006;88:163106. doi:10.1063/1.2196057.
- [32] Zickler GA, Smarsly B, Gierlinger N, Peterlik H, Paris O. A reconsideration of the relationship between the crystallite size La of carbons determined by X-ray diffraction and Raman spectroscopy. *Carbon N Y* 2006;44:3239–46.  
doi:<https://doi.org/10.1016/j.carbon.2006.06.029>.
- [33] Wagner C, Riggs WM, Davis LE, Moulder JF, Muilenberg GE. *Handbook of x-ray photoelectron spectroscopy*. Minnesota: Perkin-Elmer Corporation; 1979.
- [34] Ganguly A, Sharma S, Papakonstantinou P, Hamilton J. Probing the Thermal Deoxygenation of Graphene Oxide Using High-Resolution In Situ X-ray-Based Spectroscopies. *J Phys Chem C* 2011;115:17009–19. doi:10.1021/jp203741y.
- [35] Arteaga G, Rivera-Gavidia ML, Martínez JS, Rizo R, Pastor E, García G. Methanol Oxidation on Graphenic-Supported Platinum Catalysts. *Surfaces* 2019;2. doi:10.3390/surfaces2010002.
- [36] Rivera Gavidia LM, García G, Anaya D, Querejeta A, Alcaide F, Pastor E. Carbon-supported Pt-free catalysts with high specificity and activity toward the oxygen reduction reaction in acidic medium. *Appl Catal B Environ* 2016;184:12–9. doi:10.1016/j.apcatb.2015.11.021.
- [37] García G, Roca-Ayats M, Lillo A, Galante JL, Peña MA, Martínez-Huerta M V. Catalyst support effects at the oxygen electrode of unitized regenerative fuel cells. *Catal Today* 2013;210:67–74. doi:10.1016/j.cattod.2013.02.003.
- [38] Roca-Ayats M, Herreros E, García G, Peña MA, Martínez-Huerta M V.

- Promotion of oxygen reduction and water oxidation at Pt-based electrocatalysts by titanium carbonitride. *Appl Catal B Environ* 2016;183:53–60.  
doi:10.1016/j.apcatb.2015.10.009.
- [39] García G. Correlation between CO oxidation and H adsorption/desorption on Pt surfaces in a wide pH range. The role of alkali cations. *ChemElectroChem* 2016;4:n/a--n/a. doi:10.1002/celc.201600731.
- [40] Rivera LM, García G, Pastor E. Novel graphene materials for the oxygen reduction reaction. *Curr Opin Electrochem* 2018;9:233–9.  
doi:10.1016/j.coelec.2018.05.009.
- [41] García G, González-Orive A, Roca-Ayats M, Guillén-Villafuerte O, Planes GÁ, Martínez-Huerta MV, et al. Platinum border atoms as dominant active site during the carbon monoxide electrooxidation reaction. *Int J Hydrogen Energy* 2016;41:19674–83. doi:10.1016/j.ijhydene.2016.04.145.
- [42] Bag S, Mondal B, Das AK, Raj CR. Nitrogen and sulfur dual-doped reduced graphene oxide: Synergistic effect of dopants towards oxygen reduction reaction. *Electrochim Acta* 2015;163:16–23. doi:10.1016/j.electacta.2015.02.130.

**Declaration of interests**

The authors declare that they have no known competing financial interests or personal relationships that could have appeared to influence the work reported in this paper.

The authors declare the following financial interests/personal relationships which may be considered as potential competing interests:



## Highlights

- 1.-Carbon-based materials were synthesized, characterized and studied as bifunctional oxygen electrocatalysts.
- 2.-N-doped graphene catalyst reveals the highest catalytic activity toward the ORR.
- 3.-Carbon nanofibers is the most active catalyst toward the OER and shows acceptable catalytic activity toward the ORR.
- 4.-Carbon nanofibers can be combined with other material to develop durable catalysts for practical URFC use.

**GA**